

The Convergence of 21cm Power Spectra within a 1 Gpc/h Box Simulation during the Epoch of Reionization

Andrew Caruso & Christopher Cain

The University of California Riverside

June 19, 2023

Abstract

We investigated the minimum box size necessary for simulating the 21cm radiation during the Epoch of Reionization. By performing radiative transfer simulations using a very large simulation box of 1 Gpc/h, 21cm brightness temperature fields and power spectra generated for intense models of ionizing sources, oligarchic and extremely oligarchic models. After selecting subvolumes with average densities within $1 \pm 0.1\sigma$ and performing a convergence test to measure how well the average 21cm power of each subvolume size compared to the total power of the simulation, we created violin plots for a variety of subvolume box sizes: 100 Mpc/h, 300 Mpc/h, and 500 Mpc/h. We found that a subvolume box size of 300 Mpc/h is adequate, given violin plot means of 0.033 ± 0.037 and 0.010 ± 0.029 for each model respectively. Since we chose intense source models, more apt models run with a simulation box size of 300 Mpc/h would likely capture almost all the 21cm power spectra necessary for analysis, therefore setting a general lower limit on the minimum box size.

1 Introduction

The Epoch of Reionization (EoR) is a stage in the thermal history of the early universe in which the first sources of radiation are able to ionize the prior neutral hydrogen (HI) of the intergalactic medium (IGM). However, several aspects of the EoR remain unresolved including the morphology and evolution of ionized regions, and the sources of ionizing radiation [1] [2]. Likewise, the effects of the IGM on reionization are not fully understood, especially on small scales [1].

The investigation of the EoR was recently boosted by several observations constraining the end of the EoR, including limits on the reionization optical depth observed by the Planck Collaboration et. al. [3]. Likewise, [4] used Lyman Alpha damping wing data to find that the reionization of the IGM was incomplete at $z \sim 7$. This was also observed through massive Lyman Alpha emitter surveys conducted by [5]. On the other hand, [6] found that the reionization of the IGM may be complete at $z \lesssim 6$.

One way to potentially resolve these uncertainties is by directly observing the HI regions of the EoR. This can be done by detecting the 21cm radiation during the EoR. In particular, measuring

the 21cm power spectrum will reveal the drivers or sources of ionization, such as the first stars and galaxies, including their properties and impact on the IGM [7]. Likewise, dark matter (DM) halos hosting these first sources can also be studied [8]. Furthermore, the 21cm signal shortly after the EoR may be used to understand the impact of dark matter on Baryonic Acoustic Oscillations [9]. Ultimately, understanding the evolution of the universe during the EoR using 21cm radiation may provide new constraints on the first ionizing sources and potential dark matter models and their roles during the early universe [10][11].

However, the task has been experimentally challenging due to the large foreground of later 21cm radiation [7]. Nevertheless, radio telescope interferometers such as GMRT [12], LOFAR [13], MWA [14], PAPER [15], and now HERA [16] have set constraints on the upper limits of the 21cm radiation power spectrum time [17]. The most recent limit from HERA on the brightness temperature spectrum is less than 946 mK^2 at redshift 7.9 with wavenumber 0.19 Mpc^{-1} and less than $9,166 \text{ mK}^2$ at redshift 10.4 with wavenumber 0.26 Mpc^{-1} [16]. Moreover, HERA [16] and SKA [18] are predicted to potentially observe the 21cm power spectrum for the first time.

During this search for the 21cm power from the EoR, theoretical models have become further constrained and advanced in predicting the aspects of EoR using simulations in conjunction with machine learning [19]. But one major concern remains as to how large the simulation box size must be in order to capture all the 21cm radiation power spectrum for optimal simulation environments. This remains an issue since an arbitrarily large simulation box is limited by computational power and expenses to acquire sufficient resolution, therefore making it difficult to determine the minimum size. Nevertheless, a few collaborations have explored potentially a minimum box size of approximately 250 Mpc/h [20] or 100 Mpc/h [21]. However, the question still remains open for very large simulation boxes with different simulation processes.

One way to address this question is by studying the convergence of the 21cm power at different length scales. In order to test the convergence, we performed several radiative transfer (RT) simulations using a variety of models of ionizing sources and a very large simulation size of 1 Gpc/h . Importantly, this combination of RT simulation with a large box size of 1 Gpc/h has not been investigated before.

2 Procedure

The RT simulation essentially takes dark matter halos from an N-body simulation with assigned ionizing emissivities and traces, merges, and splits light rays according to chosen parameters. The consequent ionization fronts are then tracked with consideration of self-shielding, time evolution of photo-ionization rate, and further effects. For more details, the reader is referred to [22].

2.1 Models of Ionizing Sources

A key parameter in performing the radiative transfer simulation is the model of the ionizing sources. Currently, it is unknown how the EoR depends exactly on the ionizing sources (corresponding to different sizes of dark matter halos), such as quasars, bright (rare at high redshift) galaxies, and faint (abundant at high redshift) galaxies [23], and which type of ionizing sources contribute predominantly [24]. Consequently, the simulated 21cm power spectrum may depend on the choice of the ionizing sources and thus requires the simulation to be run multiple times with different sources. Interestingly, when the the 21cm power spectrum is observed in future experiments,

it will be helpful to have simulated expectations of the 21cm power spectrum to narrow down the range of possible models of first ionizing sources of the universe [7].

We utilized three distinct ionization models: fiducial, oligarchic, and democratic. Each model differs by the choice of dark matter halo size and thus the source of ionization. The fiducial model involves halos with a minimum mass of $2 \times 10^9 M_\odot$, wherein the emissivity of ionizing radiation is proportional to each halo's luminosity. Typical simulations utilize this type of model. In contrast, the democratic model removes the emissivity dependency on luminosity for all halos. As a result, the faint galaxies contribute more to reionization than the bright galaxies. However, the democratic model's sources are currently undetectable. Lastly, the oligarchic model involves even more massive halos with a minimum mass of $2 \times 10^{10} M_\odot$. Opposite to the democratic model, the bright galaxies contribute more than the faint galaxies in the oligarchic model. Unlike both models, however, the oligarchic sources have already been detected [22].

As an illustration of each model, Figure 1 displays the geometric cross sections of the 21cm brightness temperature fields at a chosen positional cut of 10 Mpc/h, with a fixed redshift of 7.0445. Each plot obeys the same color scheme as denoted by the spectral color bar below. The very cold regions of dark blue (less than about 10 mK) correspond to the lack of 21cm radiation and are, therefore, HII (ionized hydrogen) regions rather than HI (neutral hydrogen) regions. Note that these contour maps are from the simulation with a box length of 300 Mpc/h.

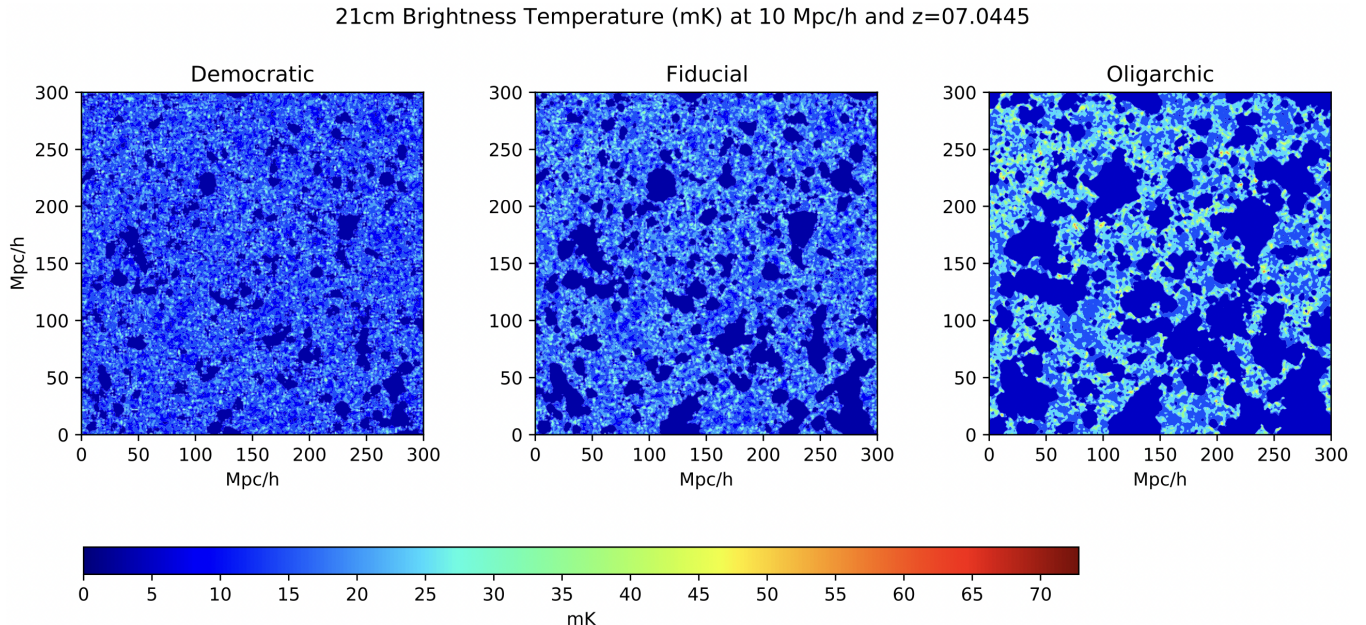


Figure 1: Brightness temperature contour maps (in units of mK) for the democratic, fiducial, and oligarchic models at redshift of 7.0445 with a chosen positional cut of 10 Mpc/h for the 300 Mpc/h length box simulation.

At redshift ~ 7 , the 300 Mpc/h box is expected to be about 50% ionized as seen in Figure 1 for each model of ionizing sources. Although the fraction of neutral to ionized gas is the same for each model, the distributions of neutral gas differ. Clearly, from Figure 1, the democratic model has smaller, more dispersed ionized bubbles (HII regions). This coincides with the fact that, in the democratic model, the faint galaxies contribution dominates over the bright galaxies. However, in the oligarchic model, the bright galaxies contribution dominates over the faint galaxies, yielding

bigger, more clustered ionized bubbles. The effect is mixed in the fiducial model, wherein both faint and bright galaxies contribute to reionization in the fiducial model, yielding an intermediate mixture of the two other models. This illustrates that depending on the source model, the topology of the HI and HII regions differ during the EoR, despite similar neutral fractions of hydrogen gas.

We also implemented a fourth model, the extreme oligarchic model, which is simply an amplification of the oligarchic model, as seen in Figure 2. As expected, the extreme model has greater more clustered ionized bubbles than the oligarchic model. We chose to use both of these oligarchic models for the 1 Gpc/h box simulation with 1024 cells, as an upper limit of the convergence test. In other words, determining the minimum converged box size for the extreme model would imply that less extreme models, such as fiducial and democratic, ought to be converged at said minimum, therefore serving as a basis for most source models. Nevertheless, the three previous models were implemented for the 300 Mpc/h box simulation with 300 cells as a forerunner to the larger volume analysis.

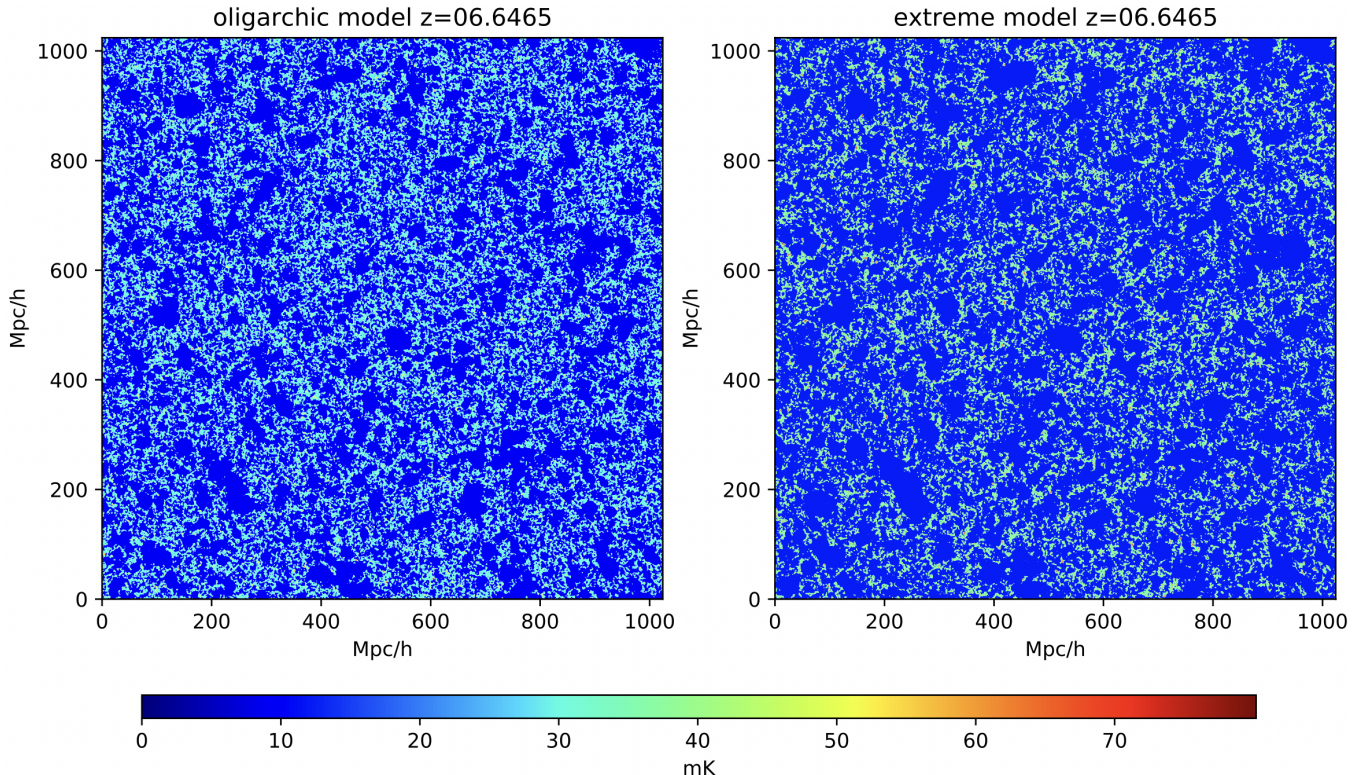


Figure 2: Brightness temperature contour maps (in units of mK) for the oligarchic and extremely oligarchic models at redshift of 6.6465 with a chosen positional cut of 10 Mpc/h for the 1 Gpc/h length box simulation.

Generally, the convergence test involved looking at the simulated 21cm power spectra of sub-volume boxes smaller than the total simulation size. Said subvolumes had to be selected carefully such that the power within a subvolume was not too small compared to the total power within the maximum simulation box size. Otherwise, small subvolumes of a particular size with significant scatter between them would likely capture too much or too little 21cm power relative to the total power in the maximum box size of the simulation.

2.2 Subvolume Selection

The simulation was performed using each model to generate the 21cm radiation brightness temperature fields for redshifts z between 4.5 and 11.8 for the 300 Mpc/h box and 6 to 10.9 for the 1 Gpc/h box. Thereafter, the power spectra was generated from the 21cm fields by performing Fast Fourier Transforms (FFT).

In order to chose the subvolumes aptly, several fixed subvolume sizes or "cuts" were selected: 100, 200, 300, 400 and 500 Mpc/h for the 1 Gpc/h box simulation and 75, 100, and 150 Mpc/h for the 300 Mpc/h box simulation. To generate many subvolumes with a particular cut, a step size (a value to repeatedly shift the entire subvolume, essentially "screening" the total simulation volume) was chosen per simulation. The step sizes were 60 Mpc/h for the 300 Mpc/h box and 128 Mpc/h for the 1 Gpc/h box. For every subvolume, we calculated the average density and only kept subvolumes with average densities within $1 \pm 0.1\sigma$, where unity corresponds to the average cosmic density (since the density data was in terms of the cosmic density) and σ was determined from taking the standard deviation of all subvolumes for a particular cut size. Without the comparison to the average cosmic density, the convergence test on random subvolumes would overestimate or underestimate unexpectedly at large redshifts or wavenumbers, which would effect the power spectra plots and thus analysis accordingly.

2.3 Convergence Test

After selecting the appropriate subvolumes for each model separately, the power spectra were generated from the 21cm brightness temperatures via the FFT. The resultant power was generated per wavenumber k at different redshifts and subvolume sizes or cuts for each model. Using all the power spectra for a single model and cut, the average power was determined at each wavenumber or redshift, alongside the standard deviation. Likewise, the power spectrum of the entire box was found and then compared to the average power spectrum from the subvolume and its corresponding deviation. This process was repeated for all the chosen cuts and again reiterated for each model.

The convergence test essentially compares the average power spectrum to the total power spectrum at different cuts and models. We created ratio plots by taking the average power, standard deviation from the average, and the total power, and dividing by the total power. For the 300 Mpc/h simulation, the smallest cut was 75 Mpc/h and the ratio plots in respect to varying wavenumber and fixed redshifts is seen in Figure 3.

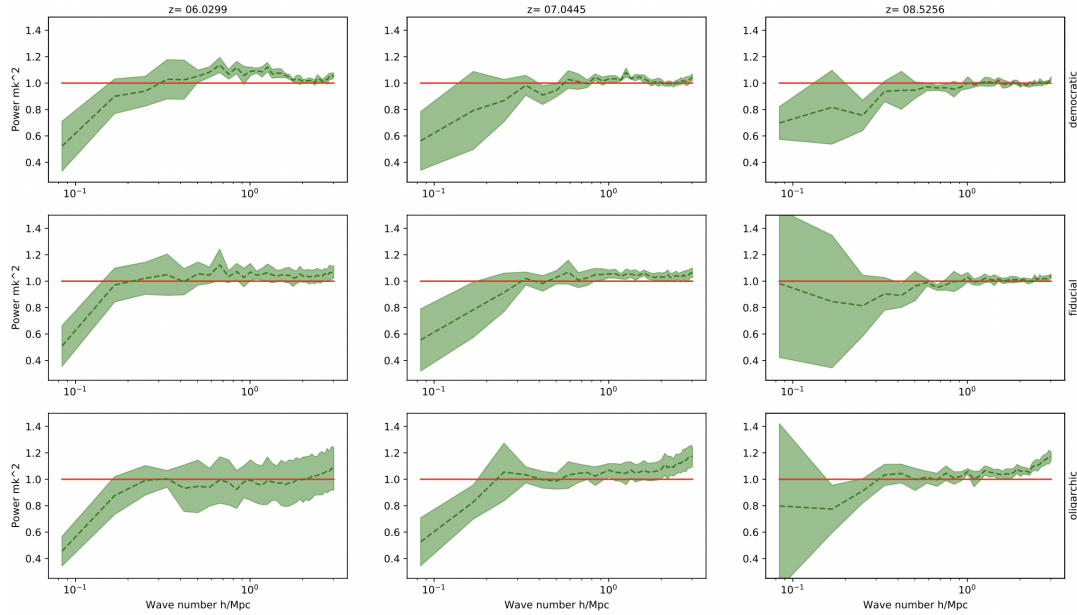


Figure 3: Ratio plots for subvolume cut of 75 Mpc/h for 300 Mpc/h box simulation. Each subplot is power in mk^2 versus wavenumber in h/Mpc , with each column being at a fixed redshift and each row corresponding to a model.

Each subplot in Figure 3 is the ratio of the average power to the total power (dash green line) with its corresponding deviation (the shaded green region), at a fixed redshift for each model. The red line denotes unity (the ratio of the total power to itself). Ultimately, the closer the average power is to unity and the more narrow the standard deviation from the average power is, the more converged the average power is to the total, thus capturing most of the 21cm power spectra at a given redshift, wavenumber, and model.

As seen in Figure 3, at very short wave numbers or very small redshifts, the average power seems to diverge rapidly from the total power. Clearly the convergence depends on the choice of redshift, wavenumber, and the model of the ionizing sources.

On the other hand, Figure 4 displays the largest subvolume cut of 150 Mpc/h with respect to wavenumber. In comparison to Figure 3, the larger subvolume has a smaller standard deviation than the smaller subvolume, as expected. Furthermore, the average power seems to be more aligned with unity for the larger subvolume, thus suggesting more convergence to the total power of the 300 Mpc/h box at each corresponding model and redshift.

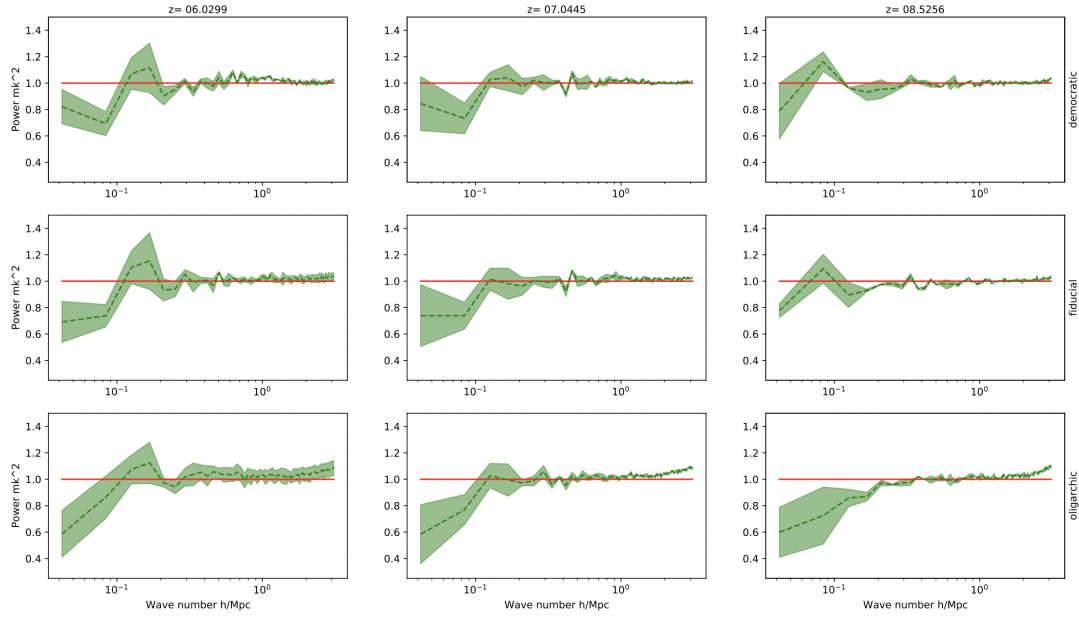


Figure 4: Ratio plots for subvolume cut of 150 Mpc/h for 300 Mpc/h box simulation. Each subplot is power in mk^2 versus wavenumber in h/Mpc , with each column being at a fixed redshift and each row corresponding to a model.

In both Figure 4 and Figure 3, it is clear that at smaller wavenumbers, the power of the subvolumes are not well converged. However, wavenumbers slightly higher than the smallest wavenumbers appear to be converged. Figure 5 displays the smallest subvolume of 75 mpc/h, however, with varying redshift at fixed wavenumbers. The subplots exhibit similar behavior to that of Figure 3.

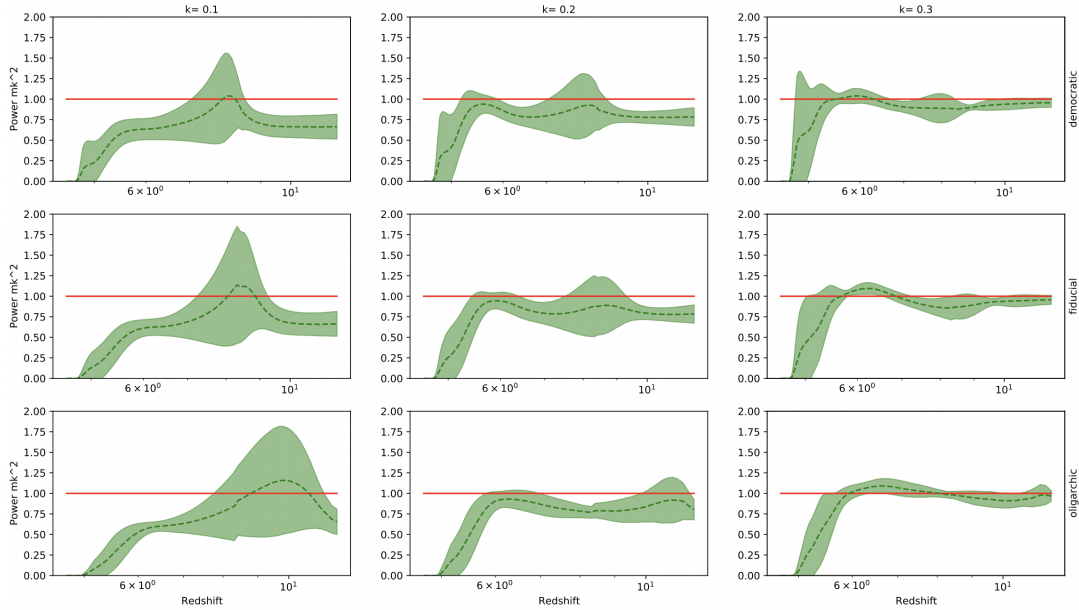


Figure 5: Ratio plots for subvolume cut of 75 Mpc/h for 300 Mpc/h box simulation. Each subplot is power in mk^2 versus redshift, with each column being at a fixed wavenumber in Mpc/h and each row corresponding to a model.

Besides the ratio plots for the 300 Mpc/h box simulation, we also acquired similar plots for the 1 Gpc/h box simulation. Figure 6 and Figure 7 display the ratio plots for the 300 Mpc/h subvolume and 100 Mpc/h subvolume cuts at fixed redshifts of 6.6465 and 6.9746.

Both exhibit similar characteristics described previously for the smaller box simulation, wherein the 300 Mpc/h cut has a tighter fit to unity and less spread deviation from the average power than the 100 Mpc/h cut.

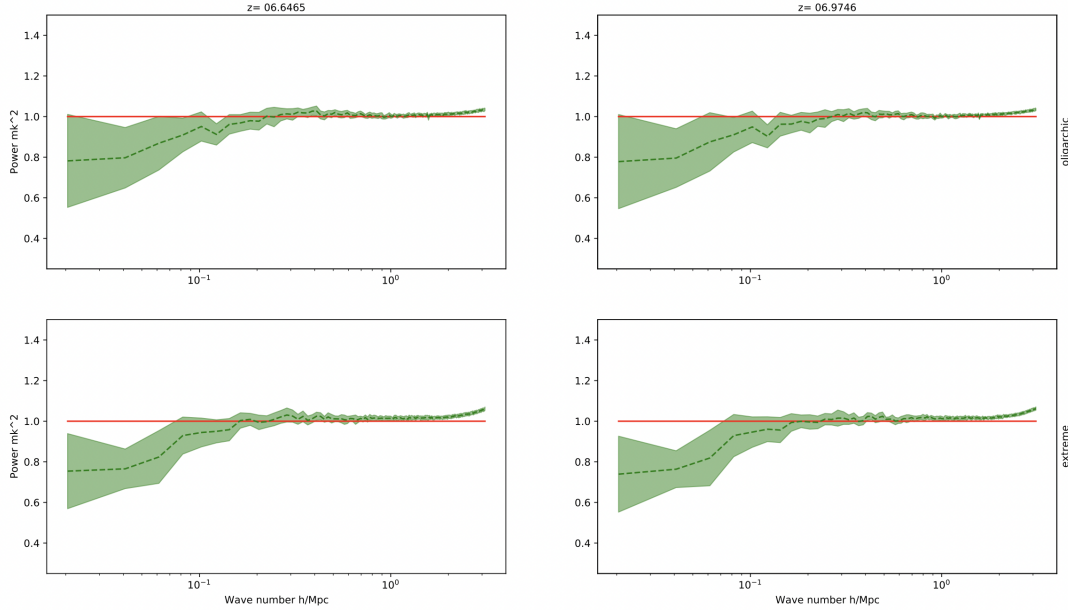


Figure 6: Ratio plots for subvolume cut of 300 Mpc/h for 1 Gpc/h box simulation. Each subplot is power in mk^{-2} versus wavenumber in h/Mpc , with each column being at a fixed redshift and each row corresponding to a model.

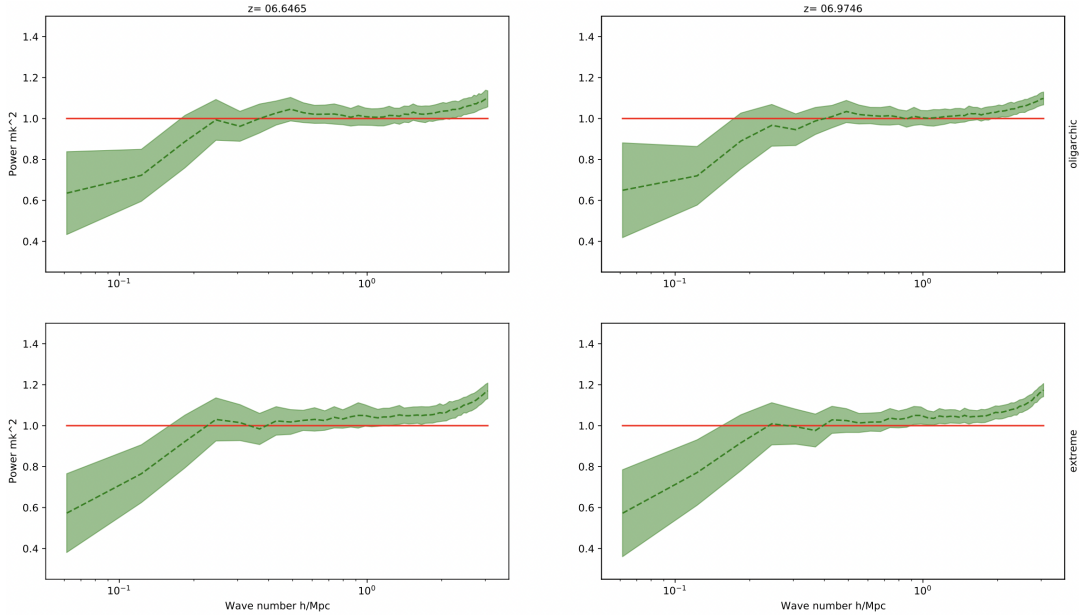


Figure 7: Ratio plots for subvolume cut of 100 Mpc/h for 1 Gpc/h box simulation. Each subplot is power in mk^2 versus wavenumber in h/Mpc , with each column being at a fixed redshift and each row corresponding to a model.

An alternative view contrasting the two cuts can be found in Figure 8 and Figure 9, which vary in respect to redshift in lieu of wavenumber. Both figures represent the ratio plots at fixed wavenumbers of 0.1, 0.2, and 0.3 h/Mpc . More clearly than the fix redshift ratio plots, Figure 6 and Figure 7, the 300 Mpc/h cut seems far more converged than the 100 Mpc/h cut, given the 100 Mpc/h cut is shifted down from unity and has a wide spread in Figure 9, compared to the opposite behavior for the 300 Mpc/h cut in Figure 8.

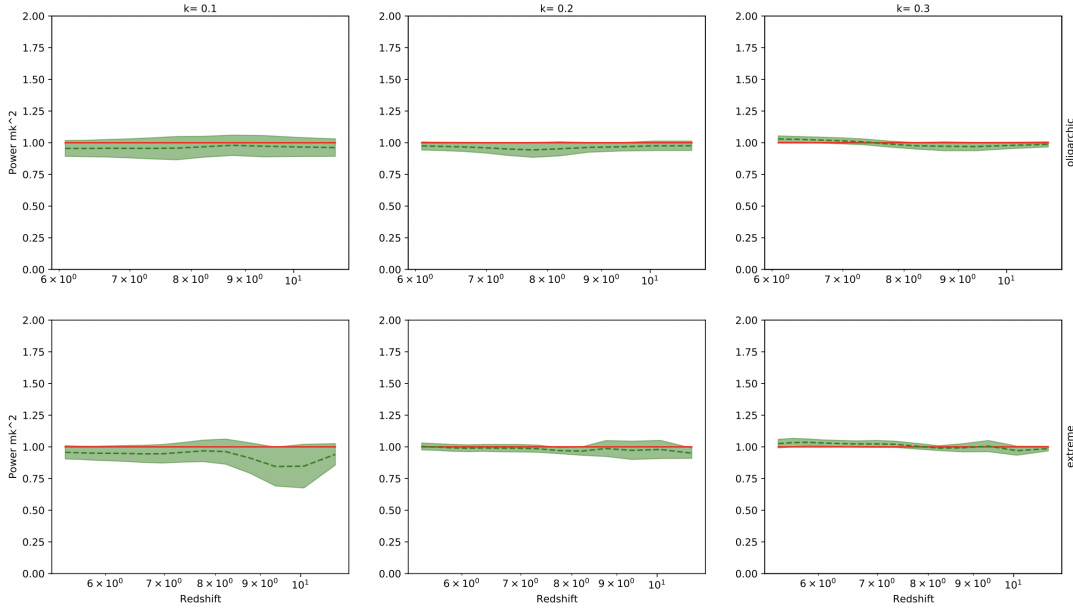


Figure 8: Ratio plots for subvolume cut of 300 Mpc/h for 1 Gpc/h box simulation. Each subplot is power in mk^2 versus redshift, with each column being at a fixed wavenumber in h/Mpc and each row corresponding to a model.

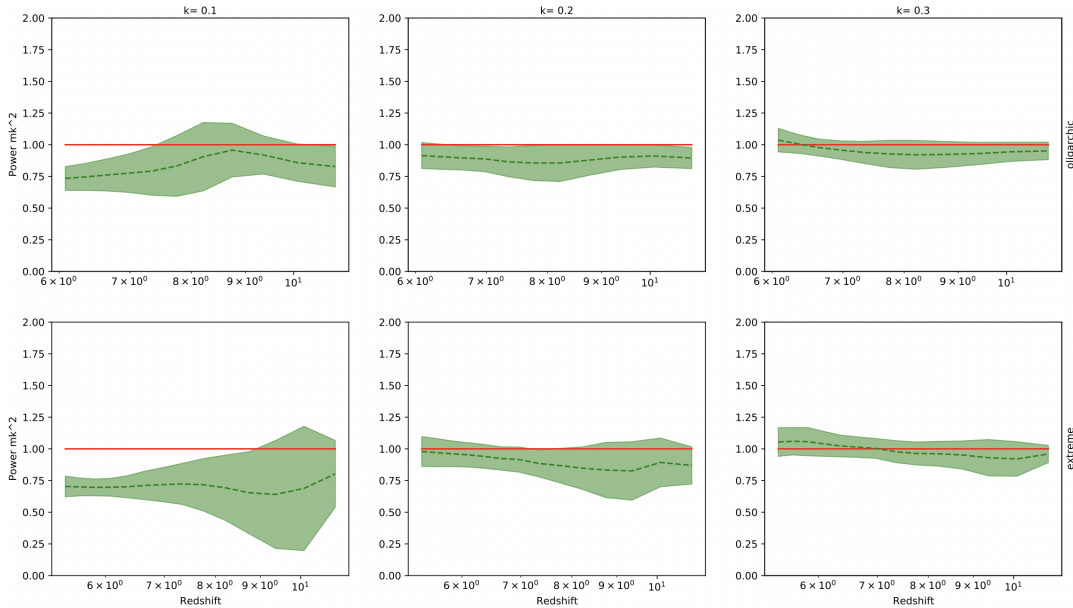


Figure 9: Ratio plots for subvolume cut of 100 Mpc/h for 1 Gpc/h box simulation. Each subplot is power in mk^2 versus redshift, with each column being at a fixed wavenumber in h/Mpc and each row corresponding to a model.

3 Results and Analysis

In order to illustrate the optimal subvolume size or cut more readily for each model in the 1 Gpc/h box simulation, we created violin plots for the oligarchic and extreme models. The chosen subvolume cuts included 100 Mpc/h, 200 Mpc/h, 300 Mpc/h, 400 Mpc/h, and 500 Mpc/h. The oligarchic model violin plot is shown in Figure 10 for fixed redshift of 6.6465 and wavenumber 0.2 Mpc/h, relevant to the EoR.¹

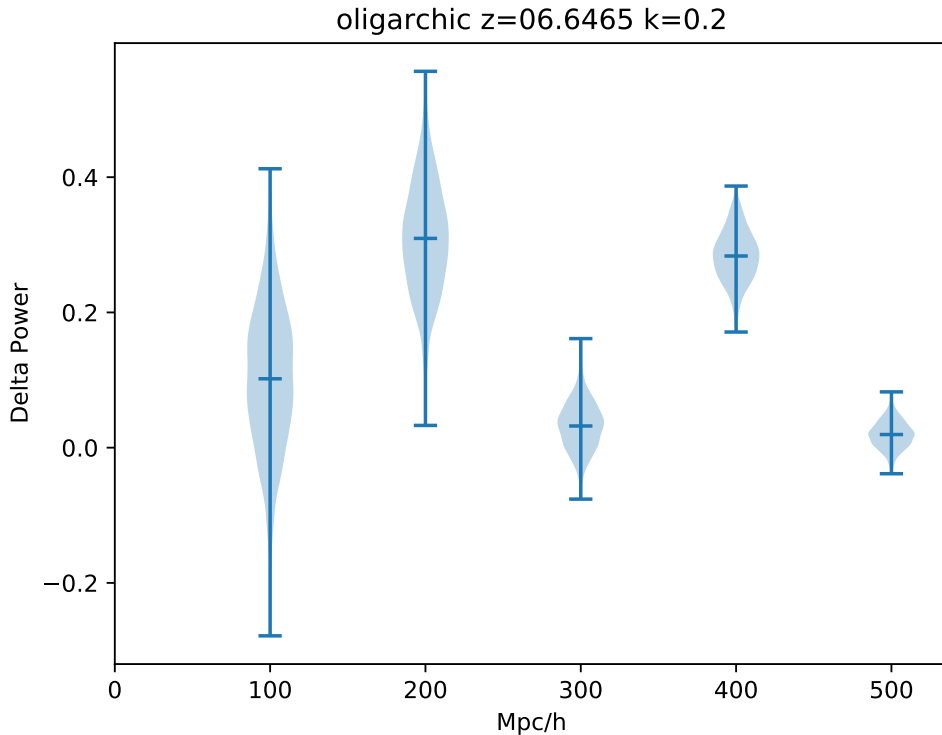


Figure 10: Violin plots for the oligarchic model in the 1 Gpc/h box simulation at fixed redshift and wavenumber with subvolume cuts of 100, 200, 300, 400, and 500 Mpc/h as labeled on the x axis.

Each violin subplot in Figure 10 represents the Gaussian distribution for each cut in Mpc/h in terms of ΔP . The Gaussian distributions utilized the standard deviation of all the power ratios (power value to the total power) and a mean ΔP as expressed in equation 1.

$$\Delta P = \left| \frac{P_{avg}}{P_{tot}} - 1 \right| \quad (1)$$

The ΔP represents the fractional difference between the average power and total power. Note that the offset of 1 was merely for plotting convenience. In equation 1, P_{avg} is the average power of all selected subvolumes for a single fixed subvolume size or cut, while P_{tot} is the total power of the 1 Gpc/h box or maximum volume of the simulation.

¹There was an issue with the 200 Mpc/h and 400 Mpc/h cuts being much greater than expected. No inconsistency in the 1 Gpc/h box code was found compared to the violin plot code for the 300 Mpc/h (which appeared good). It was suspected that the interpolation of wavenumbers was the cause, however, the issue was not resolved.

For the oligarchic model, the 300 Mpc/h cut is fairly converged, given its smaller standard deviation and more narrow distribution than other subvolume cuts in Figure 10. Moreover, the 300 Mpc/h mean is close to zero, implying that the average power is approximately equal to the total power of the simulation box. To be precise, the 300 Mpc/h cut had a mean of 0.033 ± 0.037 , while the means for the 100 Mpc/h and 500 Mpc/h cuts were 0.104 ± 0.106 and 0.019 ± 0.020 , respectively.

Although the 500 Mpc/h cut is technically more converged, the 300 Mpc/h cut is sufficiently converged, given the difference between the two cuts is relatively small. Likewise, the 100 Mpc/h is apparently not well converged, thus indicating that the minimum converged box size, at least with the selected cuts, is 300 Mpc/h.

A similar trend appears for the extremely oligarchic model in Figure 11, which has means of 0.010 ± 0.029 , 0.076 ± 0.099 , and 0.022 ± 0.020 for the 300 Mpc/h, 100 Mpc/h cuts, and 500 Mpc/h cuts respectively. Consequently, our result of a minimum box size of 300 Mpc/h is in similar agreement with the 250 Mpc/h box size from [20].

Duly note, however, that the violin plots do not contain subvolume cuts greater than 500 Mpc/h. Therefore, we can only infer that box sizes greater are sufficiently or far more converged to the total power of the 1 Gpc/h box. Nevertheless, the subvolumes do not converge sufficiently until, in this case, a subvolume of 300 Mpc/h.

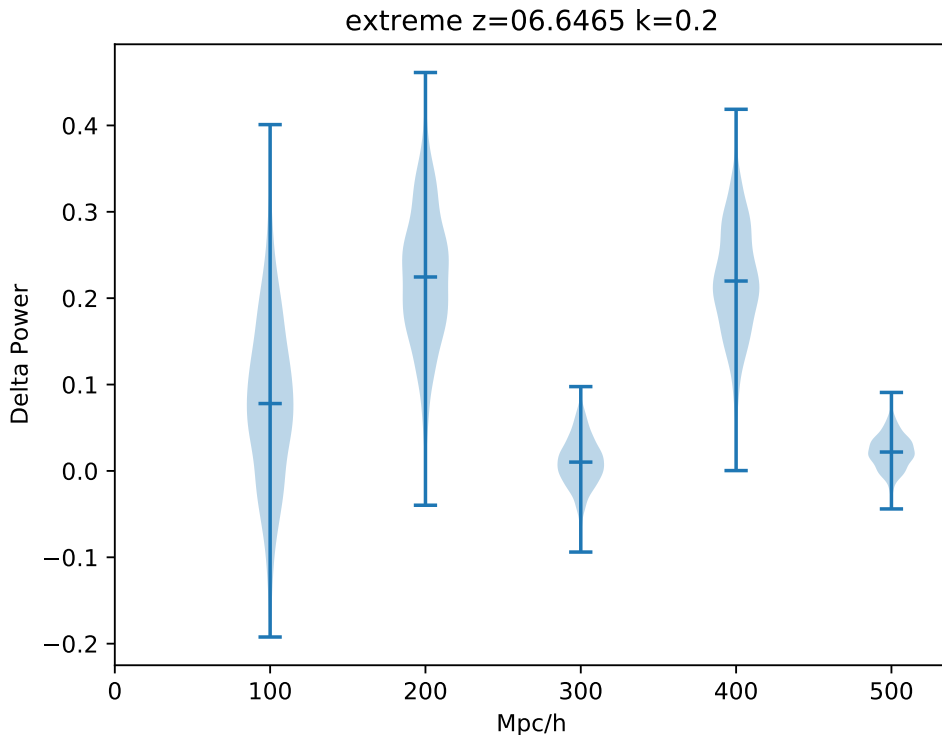


Figure 11

4 Conclusion

Consequently, we found that for the 1 Gpc/h box simulation, the convergence test for both the oligarchic and extremely oligarchic models yielded a converged 300 Mpc/h cut, with a mean of 0.033 ± 0.037 and 0.010 ± 0.029 , respectively. Id est, subvolumes below 300 Mpc/h do not converge enough and subvolumes greater than 300 Mpc/h sufficiently converge, thus placing an approximate lower threshold on simulation box size.

Since the oligarchic and extremely oligarchic models are intense models of ionizing sources, the choice of choice of a 300 Mpc/h simulation box to capture a significant amount of 21cm radiation power is also acceptable for more reasonable models such as fiducial and democratic models.

Nevertheless, further analysis of a large simulation box of the 21cm radiation using less intense models may be necessary to better constrain the minimum box size needed to encapsulate a significant amount of the total 21cm power. Likewise, more subvolume sizes or cuts can be selected, such that the window of the threshold is much smaller and more precise.

The analysis herein, has provided some illumination as to how large a simulation box must be to adequately analyze the 21cm radiation from the EoR. Furthermore, the general methods may also be applicable in looking at other parameters associated with the EoR, to further constrain simulation size. The ultimate effort will be to create better simulations prior to the first detection of the 21cm radiation from the EoR in order to easily and rapidly pinpoint theoretical models regarding the EoR.

5 Acknowledgements

This paper served as the senior thesis for Andrew Caruso for his undergraduate senior thesis at the University of California Riverside (UCR). Thus, a few important acknowledgements ought to be expressed in gratitude of undertaking this project.

Recognition goes foremost to the supervisor, Chris Cain, the graduate researcher who ran the simulations per se and over-viewed the data analysis performed by Andrew Caruso.

Furthermore, the project was completed under the principal investigator, Professor Anson D'Aloisio at the University of California Riverside, of whom this project would not have transpired without. Andrew would like to recognize Professor D'Aloisio for the opportunity to partaken in this theoretical cosmological research with Chris and for inspiring curiosity in astrophysics and cosmology in Andrew's future field of interest: theoretical astroparticle physics.

References

- [1] A. D'Aloisio, M. McQuinn, H. Trac, C. Cain, and A. Mesinger, "Hydrodynamic Response of the Intergalactic Medium to Reionization," *Astrophys. J.*, vol. 898, no. 2, p. 149, 2020.
- [2] A. Jeeson-Daniel, B. Ciardi, and L. Graziani, "Clumping factors of HII, HeII and HeIII," *Mon. Not. Roy. Astron. Soc.*, vol. 443, no. 3, pp. 2722–2732, 2014.
- [3] N. Aghanim *et al.*, "Planck 2018 results. VI. Cosmological parameters," *Astron. Astrophys.*, vol. 641, p. A6, 2020. [Erratum: *Astron. Astrophys.* 652, C4 (2021)].
- [4] B. Greig, A. Mesinger, Z. Haiman, and R. A. Simcoe, "Are we witnessing the epoch of reionization at $z=7.1$ from the spectrum of J1120+0641?," *Mon. Not. Roy. Astron. Soc.*, vol. 466, no. 4, pp. 4239–4249, 2017.
- [5] W. Hu, J. Wang, Z.-Y. Zheng, S. Malhotra, J. E. Rhoads, L. Infante, L. F. Barrientos, H. Yang, C. Jiang, W. Kang, L. A. Perez, I. Wold, P. Hibon, L. Jiang, A. A. Khostovan, F. Valdes, A. R. Walker, G. Galaz, A. Coughlin, S. Harish, X. Kong, J. Pharo, and X. Zheng, "The Ly α luminosity function and cosmic reionization at $z \sim 7.0$: A tale of two lager fields," *The Astrophysical Journal*, vol. 886, p. 90, nov 2019.
- [6] Y. Zhu *et al.*, "Chasing the Tail of Cosmic Reionization with Dark Gap Statistics in the Ly α Forest over $5 < z < 6$," *Astrophys. J.*, vol. 923, no. 2, p. 223, 2021.
- [7] A. Liu, L. Newburgh, B. Saliwanchik, and A. Slosar, "Snowmass2021 Cosmic Frontier White Paper: 21cm Radiation as a Probe of Physics Across Cosmic Ages," 3 2022.
- [8] A. Loeb and J. B. Munoz, "The First Stars May Shed Light on Dark Matter," *APS Physics*, vol. 11, p. 69, 2018.
- [9] H. Long, J. J. Givans, and C. M. Hirata, "Streaming velocity effects on the post-reionization 21-cm baryon acoustic oscillation signal," *Mon. Not. Roy. Astron. Soc.*, vol. 513, no. 1, pp. 117–128, 2022.
- [10] J. Mirocha, J. B. Muñoz, S. R. Furlanetto, A. Liu, and A. Mesinger, "A galaxy-free phenomenological model for the 21-cm power spectrum during reionization," *Mon. Not. Roy. Astron. Soc.*, vol. 514, no. 2, pp. 2010–2030, 2022.
- [11] F. List, P. J. Elahi, and G. F. Lewis, "Lux ex tenebris: The imprint of annihilating dark matter on the intergalactic medium during Cosmic Dawn," *Astrophys. J.*, vol. 904, no. 2, p. 153, 2020.
- [12] G. Paciga *et al.*, "A refined foreground-corrected limit on the HI power spectrum at $z=8.6$ from the GMRT Epoch of Reionization Experiment," *Mon. Not. Roy. Astron. Soc.*, vol. 433, p. 639, 2013.
- [13] F. G. Mertens *et al.*, "Improved upper limits on the 21-cm signal power spectrum of neutral hydrogen at $z \approx 9.1$ from LOFAR," *Mon. Not. Roy. Astron. Soc.*, vol. 493, no. 2, pp. 1662–1685, 2020.
- [14] N. Barry *et al.*, "Improving the Epoch of Reionization Power Spectrum Results from Murchison Widefield Array Season 1 Observations," 9 2019.

- [15] M. Kolopanis *et al.*, “A simplified, lossless re-analysis of PAPER-64,” 9 2019.
- [16] Z. Abdurashidova *et al.*, “Improved Constraints on the 21 cm EoR Power Spectrum and the X-Ray Heating of the IGM with HERA Phase I Observations,” *Astrophys. J.*, vol. 945, no. 2, p. 124, 2023.
- [17] A. Pathak, S. Bag, S. Dasgupta, S. Majumdar, R. Mondal, M. Kamran, and P. Sarkar, “Distinguishing reionization models using the largest cluster statistics of the 21-cm maps,” *JCAP*, vol. 11, p. 027, 2022.
- [18] D. Vrbanec, B. Ciardi, V. Jelic, H. Jensen, I. T. Iliev, G. Mellema, and S. Zaroubi, “Predictions for the 21cm–galaxy cross-power spectrum observable with SKA and future galaxy surveys,” *Mon. Not. Roy. Astron. Soc.*, vol. 492, no. 4, pp. 4952–4958, 2020.
- [19] C. S. Murmu, R. Ghara, S. Majumdar, and K. K. Datta, “Probing the epoch of reionization using synergies of line intensity mapping,” *J. Astrophys. Astron.*, vol. 43, no. 2, p. 104, 2022.
- [20] H. D. Kaur, N. Gillet, and A. Mesinger, “Minimum size of 21-cm simulations,” 4 2020.
- [21] I. T. Iliev, G. Mellema, K. Ahn, P. R. Shapiro, Y. Mao, and U.-L. Pen, “Simulating cosmic reionization: How large a volume is large enough?,” *Mon. Not. Roy. Astron. Soc.*, vol. 439, no. 1, pp. 725–743, 2014.
- [22] C. Cain, A. D’Aloisio, N. Gangolli, and M. McQuinn, “The Morphology of Reionization in a Dynamically Clumpy Universe,” 7 2022.
- [23] A. Bera, S. Hassan, A. Smith, R. Cen, E. Garaldi, R. Kannan, and M. Vogelsberger, “Bridging the Gap between Cosmic Dawn and Reionization favors Faint Galaxies-dominated Models,” 9 2022.
- [24] A. K. Shaw *et al.*, “Probing early Universe through redshifted 21-cm signal: Modeling and observational challenges,” *J. Astrophys. Astron.*, vol. 44, no. 1, p. 4, 2023.